Epigallocatechin-3-gallate adsorbed on core–shell gold nanorod@mesoporous silica nanoparticles, an antioxidant nanomaterial with photothermal properties

Javier Avendaño-Godoy, Xavier Cattoën, Marcelo J. Kogan, Javier Morales Valenzuela

Epigallocatechin-3-gallate adsorbed on core–shell gold nanorod@ mesoporous silica nanoparticles, an antioxidant nanomaterial with photothermal properties

Javier Avendaño-Godoy[abc], Xavier Cattoën[c], Marcelo J. Kogan[a*], Javier Morales Valenzuela[b*].

[a]Departamento de Química Farmacológica y Toxicológica, Facultad de Ciencias Químicas y Farmacéuticas, Universidad de Chile, Chile.

[b]Departamento de Ciencias y Tecnología Farmacéuticas, Facultad de Ciencias Químicas y Farmacéuticas, Universidad de Chile, Chile.

[c]Université Grenoble Alpes, CNRS, Grenoble INP, Intitut Néel, France.

*Corresponding authors at:

Departamento de Ciencias y Tecnología Farmacéuticas, Facultad de Ciencias Químicas y Farmacéuticas, Universidad de Chile, Chile. *E-mail addresses*: mkogan@ciq.uchile.cl

Departamento de Química Farmacológica y Toxicológica, Facultad de Ciencias Químicas y Farmacéuticas, Universidad de Chile, Chile. *E-mail addresses*: javiermv@ciq.uchile.cl

Abstract

Epigallocatechin-3-gallate (EGCG) exhibits several pharmacological activities with potential benefits for human health, however, its use is limited by its low oral bioavailability, due to its poor stability in the gastrointestinal tract, metabolism by intestinal bacteria, and limited intestinal permeability. One promising approach to overcome these limitations is to transport the EGCG in a nanostructured system to protect it until its arrival at the site of action. In this sense, core-shell nanoparticles corresponding to gold nanorods (GNR) coated with mesoporous silica ($mSiO_2$) may be an excellent alternative combining controlled targeted drug delivery, and photothermal therapy. The aim of this work was to synthesize GNR@$mSiO_2$-NH_2 nanoparticles loaded with EGCG as a useful antioxidant material and to study their photothermal stability for their potential use in chemo-photothermal therapy. Using an initial concentration of EGCG and GNR@$mSiO_2$-NH_2 of ≥ 300 µg/mL and 1 nM, respectively, the maximum encapsulation efficiency of EGCG (19.2%) and the maximum adsorption of EGCG on the NPs (64.4 mg/g of NPs or 160.9 mg/g of $mSiO_2$, equivalent to a loading capacity of 6.0 and 13.9%, respectively). The adsorption process was adjusted to a pseudo-second-order kinetic model and the analysis of the adsorption isotherms revealed that it is a chemical adsorption. Routine tests were carried out to study the antioxidant activity of the nanosystem: DPPH• radical assay (DPPH• free radical scavenging capacity) and the Fe^{2+}-ferrozine complex formation inhibition assay (Fe^{2+} chelating capacity). The RSA of the GNR@$mSiO_2$-NH_2/EGCG nanosystem was 60.7 ± 6.9% at an EGCG equivalent concentration of 1 µg/mL and the chelating activity was 71.0 ± 6.4% at an EGCG equivalent concentration of 30 µg/mL. EGCG, as well as its RSA and chelating activity, remained stable under NIR irradiation (808 nm, 7 W/cm^2), and upon heating (up to 41°C), and under both conditions simultaneously. While the morphology and the UV-Vis-NIR spectrum of the GNR@$mSiO_2$ remained intact after being irradiated with NIR, although ultrasmall gold NPs could be observed, probably the product of photocracking of the GNR. In summary, the GNR@$mSiO_2$-NH_2/EGCG nanosystem has good antioxidant properties and remains stable against NIR irradiation, making it potentially useful for the chemo-photothermal therapy.

Keywords: *Nanoparticles, GNR@$mSiO_2$, NIR, epigallocatechin-3-gallate, adsorption, antioxidant.*

1. Introduction

Epigallocatechin-3-gallate is one of the main phenolic compounds in green tea [3]. Its anticancer activity [4] and its ability to deactivate free radicals (including those biologically relevant such as OH•, $O_2^{\bullet -}$ and H_2O_2) [5-8], chelate metals [9-12], and modulate the aggregation of proteins that are highly relevant in neurodegenerative diseases have been described [13-16]. Clinical safety trials conducted to date have shown that oral administration is well tolerated (800 mg/day with food) and safe, only minor adverse effects (nausea, dizziness, heartburn, and stomach pain) have been reported [17]. However, its use in pharmaceuticals is limited due to its low oral bioavailability, due to its poor stability in the gastrointestinal tract, metabolism by intestinal bacteria, and limited intestinal permeability [18-21]. These limitations mean that after oral or even parenteral administration, a low percentage of the EGGC dose reaches its site of action intact and functional [20, 22]. Due to this, high doses are necessary to achieve a therapeutic effect and effective treatment, which brings with it adverse effects [17]. To overcome these limitations, it is necessary to transport the drug in a nanostructured system to protect it until its arrival at the site of action.

Core-shell NPs have received considerable attention as nanocarriers for controlled and targeted drug delivery applications [23]. In this sense, core-shell NPs (*ca* 100 nm) composed of gold nanorods (GNR) coated with mesoporous silica ($mSiO_2$) are of particular interest. Indeed, the outer layer of $mSiO_2$ features a biocompatible, highly accessible and porous surface that can be easily functionalized, while the pores can be loaded with a drug for potential spatially controlled drug release [24-27]. On the other hand, the GNR core benefits from the localized surface plasmon resonance (LSPR) phenomenon that enables the absorption of light followed by the complete dissipation of the energy in the form of heat, which is known as the photothermal effect. The longitudinal plasmonic band of the GNR is located in the biological transparency window (NIR 670-900 nm) and its position can be tuned depending on its aspect ratio. Since biological tissues and fluids have minimal absorption at this wavelength, the light can penetrate deep into human tissues without causing damage, be absorbed by GNR causing a local temperature increase [28, 29]. This photothermal effect makes it possible to trigger spatial and temporal controlled release of drugs from delivery systems and, at the same time, could be useful for photothermal therapy [24, 26, 30-32].

In summary, the core-shell nanosystems based on GNR@$mSiO_2$ can be useful for chemo-photothermal therapy applications, as demonstrated by the significant number of publications devoted to cancer treatment using this type of nanosystems loaded with doxorubicin and other molecules [26, 27, 30, 33, 34]. This opens up an important range of possible diseases that can be treated by chemo-photothermal therapy by loading this core-shell nanosystem with other drugs.

The combined light-triggered-phototherapy/drug delivery strategy [24, 26] may be very useful in the particular case of EGCG, as it would enable the protection of the fragile therapeutic molecules in addition to the localized delivery for applications aimed at treating cancer or neurodegenerative diseases.

The aim of the present work is to synthesize core-shell NPs GNR@$mSiO_2$-NH_2 loaded with EGCG as a useful antioxidant material and to study their photothermal stability for their potential use in chemo-photothermal therapy. Specifically, we characterized the adsorption kinetics of EGCG and adsorption isotherms on GNR@$mSiO_2$-NH_2. In addition, the antioxidant activity of the nanosystem was characterized through DPPH• radical assay to evaluate the DPPH• free radical scavenging capacity and the Fe^{2+}-ferrozine complex formation inhibition assay to evaluate Fe^{2+} chelating capacity. Finally, the photothermal stability of the core-shell NPs and EGCG was studied.

2. Materials and Methods

2.1. Reagents, chemicals, and solvents

Epigallocatechin-3-gallate (EGCG, ≥80%), Tetrachloroauric (III) acid trihydrate ($HAuCl_4$, 99.5%), sodium borohydride ($NaBH_4$, ≥98%), L-ascorbic acid (≥99.5%), silver nitrate ($AgNO_3$, ≥99%)**,** tetraethyl orthosilicate (TEOS, 98%), (3-aminopropyl)triethoxysilane (APTES, ≥98%), cetyltrimethylammonium bromide (CTAB, ≥98%), 5,6-diphenyl-3-(2-pyridyl)-1,2,4-triazine-4′,4′′-disulfonic acid sodium salt (ferrozine, ≥97%), iron(II) chloride tetrahydrate ($FeCl_2 \cdot 4H_2O$, 98%), 2,2-diphenyl-1-picryl-hydrazyl (DPPH•), and trifluoroacetic acid (TFA, for HPLC ≥99%) were purchased from Sigma-Aldrich. Ethanol (HPLC grade), methanol (HPLC grade), and acetonitrile (HPLC grade) were obtained from Merck. Ultra-pure water (18.2 MΩ cm) was produced using a Simplicity System from

Millipore (Bedford, MA, USA). All materials were used as received without any further purification.

2.2. GNR@mSiO$_2$-NH$_2$ preparation.

The GNRs were synthesized using the seed-mediated method as described by Jara-Guajardo with minor modifications [35, 36]. For the synthesis, a seed solution and a growth solution were prepared at 27 °C. For the preparation of a seed solution, 300 µL of a freshly-prepared cold $NaBH_4$ aqueous solution (10 mM) were added to an aqueous solution containing CTAB (0.1 M, 4.7 mL) and $HAuCl_4$ (42.5 mM, 42.5 µL) under vigorous magnetic stirring. Then, a growth solution was prepared by mixing aqueous solutions of CTAB (0.1 M, 50 mL), $HAuCl_4$ (29.4 mM, 42.5 µL), ascorbic acid (0.1 M, 375 µL) and $AgNO_3$ (5 mM, 400 µL) under vigorous magnetic stirring. Finally, 600 µL of the previously prepared seed solution was added to this growth solution. The final solution was incubated for 30 min at 27 °C and centrifuged at 13,600 rcf for 20 min. After centrifugation, the supernatant was removed and the pellet was resuspended in water. The centrifugation procedure was repeated at 11,200 rcf for 20 min to remove excess CTAB. The pellet was finally resuspended in 50 mL of water.

Coating of mesoporous silica ($mSiO_2$) on bare GNR was achieved by a modified Stöber method in accordance with previous reports with minor modifications [37]. Briefly, to the previous suspension (50 mL) was added a CTAB solution (0.1 M, 200 µL) to reach a CTAB concentration of 0.4 mM. After 20 h of stirring, NaOH (0.1 M, 200 µL) was added and after an additional 30 min of stirring three aliquots of TEOS in methanol (20% (v/v), 3*150 µL) were added at 30 min intervals with magnetic stirring. The mixture was stirred for 20 h and washed three times with water by centrifugation (6,080 rcf for 30 min) to remove the CTAB templates and finally, the GNR-$mSiO_2$ were resuspended in ethanol (50 mL).

Amino-functionalization of the GNR@$mSiO_2$ was performed by adding 1 mL of APTES under magnetic stirring for 20 h. Then, the NPs were washed three times with ethanol by centrifugation (6,080 rcf for 20 min), and finally resuspended in ethanol.

2.3. Characterization of GNR@mSiO$_2$-NH$_2$

UV-Vis-NIR absorption spectra were determined in ethanol using a Perkin Elmer Lambda 25 spectrophotometer.

Dynamic light scattering (DLS) characterization, which provides information regarding the hydrodynamic diameter (D_h) of the NPs, was performed using a Malvern ZetaSizer Nano ZS90 (Malvern, UK). For DLS analysis, a 1 mL aliquot of each solution was placed in a disposable polycarbonate cell (DTS 1070, Malvern, UK) under precise temperature control (25 °C) in ethanol. The hydrodynamic diameter was derived from the autocorrelation function by means of the Stokes-Einstein equation [38].

Zeta potential (ZP) measurements were performed on a Malvern ZetaSizer Nano ZS90 (Malvern, UK). Disposable polycarbonate cells (DTS 1070, Malvern, UK) were used under precise temperature control (25 °C) in ethanol. The ZP was calculated from the mean electrophoretic mobility using the Smoluchowski approximation [38].

The morphology of GNR@$mSiO_2$ was determined by transmission electron microscopy (TEM), using a Hitachi HT-7700 electron microscope (HV: 120 kV). Images were processed with the ImageJ program to determine $mSiO_2$ layer thickness and dimensions of GNR and GNR@$mSiO_2$. High-resolution TEM (HR-TEM) images for the study of the photothermal stability of GNR@$mSiO_2$ were obtained using a JEOL JEM 2100 electron microscope (HV: 200 kV).

Fourier transform infrared (FT-IR) spectra were obtained on an Interspec 200-X FT-IR spectrometer with a resolution of 4 cm^{-1}, in the range 600-4000 cm^{-1}, with an average of 16 scans.

Differential scanning calorimetry (DSC) curves for GNR@$mSiO_2$, GNR@$mSiO_2$-NH_2, EGCG, physical mixture GNR@$mSiO_2$-NH_2 + EGCG, and GNR@$mSiO_2$-NH_2/EGCG were obtained from a NETZSCH DSC 3500 system (NETZSCH, Germany). Scanning was performed between 20 and 300 °C with a heating rate of 5 °C/min.

N_2-sorption isotherms were recorded at the University of Montpellier, France, on a Micromeritics 3Flex apparatus, after outgassing for 18 h at 80 °C. Owing to the low amount of material analyzed (6.7 mg), uncertainties on the weight (± 0.5 mg) give errors of ± 8% for the specific surface area and pore volume.

2.4. Chromatographic method

Chromatographic analysis was performed using a Shimadzu Prominence HPLC system (Kyoto, Japan) composed of LC-20AT pump, DGU-$20A_{5R}$ degassing unit, CTO-20A column

oven, SIL-20A autosampler and SPD-M20A diode array detector. Data were acquired, recorded and analyzed by means of Shimadzu LabSolutions 5.54 software. The separation was carried out on an IntertSustain C-18 column (GL Science Inc.; 4.6 mm × 250 mm; particle size 5 µm; carbon load 14%; surface area 200 m^2/g; pore size 100 Å; pH stability 1-10) at room temperature. A binary mobile phase composed of water acidified with 0.1% v/v trifluoroacetic acid (solvent A) and acetonitrile (solvent B) was used. The determinations were carried out in an isocratic elution mode using 80% v/v of solvent A at a flow of 1 mL/min. The injection volume was 15 µL and detection was carried out by UV absorption at 280 nm. EGCG was detected at 7.25 min during a total run time of 12 min. The optimized method was validated both in ethanol and in water following the guidelines of the International Conference on Harmonization (ICH) [39] (Sections 2 and 3 of the Supplementary Material).

2.5. EGCG adsorption on GNR@mSiO₂-NH₂

The adsorption was evaluated by adding different volumes of an ethanolic EGCG solution (2 mg/mL) to ethanolic solutions of GNR@mSiO$_2$-NH$_2$ in a 1 mL volumetric flask to obtain different final EGCG concentrations (70, 100, 150, 200, 300, 400, and 500 µg/mL) and a constant final concentration of GNR@mSiO$_2$-NH$_2$ equal to 1 nM. Then, the final solutions were stirred for 24 h at room temperature (25 ºC) to reach adsorption equilibrium and subsequently centrifuged at 6,080 rcf for 30 min [40]. The supernatant was recovered and filtered (0.22 µm MCE membrane) to obtain aliquots suitable for analysis of residual EGCG concentration using the validated HPLC method of the present work (Section 2.4). The amount of EGCG adsorbed at equilibrium per unit of GNR@mSiO$_2$-NH$_2$, called q_e (mg/g), was calculated from the following equation:

$$q_e = \frac{(C_0 - C_e)\,V}{m} \qquad (\mathbf{1})$$

Where C_0 and C_e are the concentrations of EGCG in solution before and after adsorption (mg/L), respectively, V is the bulk volume of the medium (L) and m is the mass of GNR@mSiO$_2$-NH$_2$ (g).

2.6. Adsorption kinetics

The adsorption kinetics of EGCG on GNR@mSiO$_2$-NH$_2$ were evaluated by adding one volume of ethanolic EGCG solution to an ethanolic solution of GNR@mSiO$_2$-NH$_2$ in a 1 mL volumetric flask, for a final concentration of EGCG and GNR@mSiO$_2$-NH$_2$ equal to 300 µg/mL (to reach equilibrium of adsorption) and 1 nM, respectively. The final solution was kept at room temperature (25 ºC) under constant magnetic stirring. At defined time intervals (0, 0.5, 1, 4, 6, 24, 30, 48, and 54 h), samples were collected and centrifuged at 6,080 rcf for 30 min [40]. The supernatant was recovered and filtered (0.22 µm MCE membrane) to obtain aliquots suitable for analysis of residual EGCG concentration using the validated HPLC method of the present work (Section 2.4). The amount of EGCG adsorbed per unit of GNR@mSiO$_2$-NH$_2$ after each time interval, called q_t (mg/g), was calculated using the following equation:

$$q_t = \frac{(C_0 - C_t)\,V}{m} \qquad (\mathbf{2})$$

Where C_0 is the initial concentration of EGCG (mg/L) and C_t is the concentration at a time "t" (mg/L), V and m have the same meaning as in equation (1).

2.7. Antioxidant activity evaluation

2.7.1. DPPH• Radical Assay

The DPPH• radical assay was performed as described by Arriagada et al. [41]. Briefly, 1 mL of freshly prepared DPPH• (50 µM) solution in methanol was mixed in a 5 mL amber volumetric flask with different volumes of an EGCG solution, either free or adsorbed to GNR@mSiO$_2$-NH$_2$, using a final concentration range from 0.05-1 µg/mL. The samples were shaken for 20 min at room temperature (25 ºC), then the samples were centrifuged at 14,850 rcf for 15 min and the supernatant was analyzed spectrophotometrically at 515 nm. The radical-scavenging activity (RSA), expressed as a percentage, was calculated according to the following equation:

$$RSA\ (\%) = \frac{A_0 - A_1}{A_0} \times 100 \qquad (\mathbf{3})$$

Where A_0 corresponds to the absorbance of the control (without EGCG or NPs) and A_1 is the absorbance of the sample.

2.7.2. Measurements of chelating activity

The chelating activity of free and adsorbed EGCG on GNR@mSiO$_2$-NH$_2$ were studied based on their ability to inhibit the formation of the Fe^{2+}-ferrozine complex, as described by Arriagada et al. [41]. In a 2 mL volumetric flask, different volumes of an EGCG solution, either free or adsorbed to GNR@mSiO$_2$-NH$_2$ (for a final concentration of 20-30 µg/mL), were mixed with 40 µL of $FeCl_2$ (2 mM) and 80 µL of ferrozine (2 mM) in a mixture of ethanol/acetate buffer (15/85, pH 5.0) and stirred for 10 min to reach equilibrium. The samples were centrifuged at 14,850 rcf for 15 min and the absorbance of the supernatant was measured at 562 nm. The chelating activity, expressed as a percentage, was calculated according to the following equation:

$$Chelating\ activity\ (\%) = \frac{A_0 - A_1}{A_0} \times 100 \qquad (\mathbf{4})$$

Where A_0 corresponds to the absorbance of the control solution containing $FeCl_2$ and ferrozine, and A_1 is the absorbance of the sample.

2.8. Stability of GNR@mSiO$_2$ and EGCG against NIR irradiation

To evaluate the stability of GNR@mSiO$_2$, the NPs were suspended in milli-Q water and subjected to NIR irradiation (808 nm, 7 W/cm^2) for 15 min. The irradiated samples were characterized by UV-Vis-NIR spectroscopy, DLS, ZP, and TEM (Section 2.3).

To evaluate the stability of EGCG, aqueous solutions (80 µg/mL) were subjected to NIR irradiation (808 nm, 7 W/cm^2; IQ1A350, PowerTechnology Inc., USA), a temperature bath (41 ºC) and both conditions simultaneously for 30 min. Samples were immediately quantified using the previously validated chromatographic method (Section 3 of the Supplementary Material). To ensure that EGCG maintains its activity after NIR irradiation, its RSA and chelating activity were evaluated after subjecting it to the same conditions mentioned above.

2.9. Statistical analysis

All determinations were performed in triplicate (n = 3) and data were evaluated using descriptive statistics [mean and standard deviation (SD), standard error of the mean (SEM), or relative standard deviation (RSD)]. Significant differences (* $p < 0.05$; ** $p < 0.01$; *** $p < 0.001$; **** $p < 0.0001$) for three or more groups were determined by analysis of variance (ANOVA) and the Tukey test. Calibrations were established by applying a linear regression model to verify linearity. Calibrations with and without matrix were compared using the F test and statistically significant differences were established for a value of $p < 0.05$. All statistical analysis was carried out with GraphPad Prism 6 (GraphPad Software, San Diego, USA).

3. Results and discussion

3.1. NPs characterization

The analysis of the TEM images of the NPs (Figure 1a), allowed determining that the length and width of the GNR were 34 ± 9 nm and GNR 9 ± 1 nm, with an average aspect ratio (length/width) of 3.7 ± 0.4 (Figures S1a, S1b, S1c of the Supplementary Material). The length and width of GNR@mSiO_2 were 79 ± 8 nm and 63 ± 6 nm (Figures S1d and S1e of the Supplementary Material), respectively. On the other hand, the thickness of the mSiO_2 shell was 29 ± 4 nm (Figure 1c). Due to the GNR concentration used, the thickness of the mSiO_2 layer depends on the CTAB concentration used [37, 42]. Using the same concentration of CTAB (0.4 mM) and GNR (≈ 1 nM), Abadeer et al. [37] obtained a thickness of 26 nm.

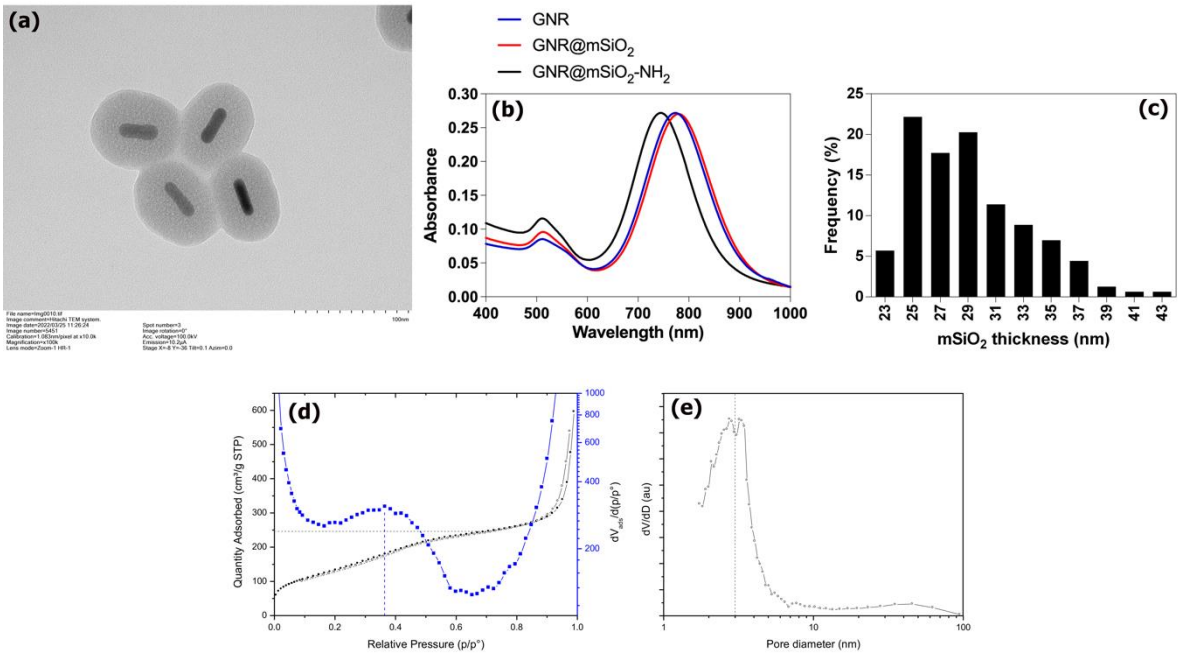

Figure 1: TEM image of GNR@$mSiO_2$ (a), UV-Vis-NIR spectra (b), thickness of the cover $mSiO_2$ corresponding to one of the samples studied (c), (black) N_2-sorption isotherm of GNR@$mSiO_2$ with (blue) first derivative of the plot (d), and BJH plot based on the desorption branch (e).

The porosity of the GNR@$mSiO_2$ was analyzed from the N_2-sorption isotherm (Figure 1d-e). The plot is typical of silica NPs obtained using CTAB as templating agent [43]. The first derivative of the plot allows to easily locate two substeps in the adsorption branch at p/p° 0.37 and 0.95. The latter is attributed to the condensation of N_2 in the large interparticular voids (30-50 nm), and is therefore not of interest for this study. The former corresponds to the filling of the inner mesopores of the silica framework, with a pore diameter of 3.0 ± 0.2 nm, as inferred from the Barrett-Joyner-Elmer (BJH) transform. Notably, no micropores are present as inferred from the *t*-plot analysis. The inner pore volume V_p = 0.38 ± 0.03 cm^3/g was calculated at p/p° = 0.7 after all inner pores are filled but before N_2 starts to condense in the interparticular voids. The Brunauer-Emmet-Teller (BET) method yielded a specific surface area of 510 ± 40 m^2/g. The pore volume [44, 45] and specific surface [25, 46-48] values are similar to those reported in other works for GNR@$mSiO_2$. These values may seem low, one has to keep in mind that GNR@$mSiO_2$ are made of dense gold cores covered by $mSiO_2$ layers. A simple geometric calculation based on the dimensions of the cores and of

the whole NPs shows that gold accounts for *ca* 60% of the weight. Therefore, the pore volume and specific surface area for the $mSiO_2$ part only of these NPs are around 0.95 cm^3/g and 1200 m^2/g, which are usual values for mesoporous silica obtained using CTAB as templating agent [49].

The process of synthesis, amino-functionalization and loading of the core-shell nanosystem with EGCG was followed by DLS, electrophoretic mobility (Table S1 of the Supplementary Material) and UV-Vis-NIR spectroscopy (Figure 1b). The GNR@$mSiO_2$ presented a negative ZP equal to -23 ± 2 mV attributed to the $mSiO_2$ shell [24, 50] and a longitudinal and transverse plasmonic band of 782 ± 3 and 512 ± 1 nm, respectively, characteristics of GNR with an aspect ratio close to 3.7 [35, 37, 51]. The cumulant fit of the DLS autocorrelation function for GNR@$mSiO_2$ suspensions in ethanol yielded values of 131 ± 8 and 19 ± 4 nm. The largest D_h value is significantly larger than the length determined by TEM, which can be attributed to a moderate aggregation of the NPs in the suspension, while the lower-than-expected value for the transverse D_h value most probably results from the difficult multiple-component fit of autocorrelation functions [52]. The amino-functionalization of the nanosystem was verified with the change of the ZP to positive (42 ± 4 mV), and by the significant blue-shift of the longitudinal and transverse plasmon bands (730 ± 13 and 513 ± 3 nm, respectively).

After loading with EGCG, a notable decrease in ZP occurred to 4 ± 2 (Table S1 of the Supplementary Material), and a small absorption band (indicated with a red arrow) appeared near 280 nm (275 nm) in the UV-Vis-NIR absorption spectrum (Figure 2a), attributed to the presence of EGCG adsorbed on the NPs.

FT-IR spectra were recorded in the range of 600-4000 cm^{-1} (Figure 2b). The intense absorption band at 1071 cm^{-1} was attributed Si-O-Si asymmetric stretching vibrations. [24, 26, 40, 53], while the 968 cm^{-1} and 794 cm^{-1} bands are related to the Si-OH asymmetric vibration and the Si-O symmetric vibration, respectively [40, 53, 54]. Residual CTAB-related peaks can be observed as well, at 2923 cm^{-1} and 2854 cm^{-1} attributable to CH_2 asymmetric and symmetric stretching vibrations and at 1490 cm^{-1} (CH_2 bending and CH_3-(N^+) deformation) [24, 53, 55].

The spectrum of GNR@$mSiO_2$-NH_2, shows some changes compared to the spectrum of GNR-$mSiO_2$; the Si-OH asymmetric stretching band at 968 cm^{-1} decreased its intensity, in

addition the bands at 2923 cm^{-1} and 2854 cm^{-1} increased slightly due to the vibration of the CH_2 group of the propyl chain [40, 56, 57] [40]; a new band was also observed at 1559 cm^{-1} attributed to NH_2 asymmetric bending [24, 40]. This means that the concentration of Si-OH groups decreased on the surface of the NPs and the amount of NH_2 groups increased, suggesting a successful functionalization with APTES [40].

In the EGCG spectrum, characteristic absorption bands are observed at 3354 and 3280 cm^{-1} corresponding to the stretching vibrations of the phenolic -OH groups; 1691 cm^{-1} and 1616 cm^{-1} corresponding to the stretching of the C=O group of the gallate moiety [58-61]; the 1543 cm^{-1} band is attributed to the C-C stretch; the band at 1446 cm^{-1} is attributed to the C-H group of the chroman ring; the bands at 1345 and 1220 cm^{-1} represent the O-C=O group; 1146 and 1097 cm^{-1} are attributed to the -OH group; 789 cm^{-1} attributed to the C-H group of the adjacent ring of the chroman ring [58, 61, 62].

In the GNR@mSiO_2-NH_2/EGCG spectra, a weak band is observed at 1618 cm^{-1} corresponding to one of the stretching bands of the C=O group of the gallate moiety of EGCG, which confirms the adsorption of EGCG on the NPs. Furthermore, there was a decrease in the band at 1559 cm^{-1} attributed to the asymmetric bending of -NH_2 and the -OH vibration bands (3354 and 3280 cm^{-1}) of EGCG did not appear, suggesting that the amino groups on the surface of the NPs and the hydroxyls of EGCG could be involved in the adsorption process [60, 63], through the formation of hydrogen bonds and strong electrostatic interactions [64].

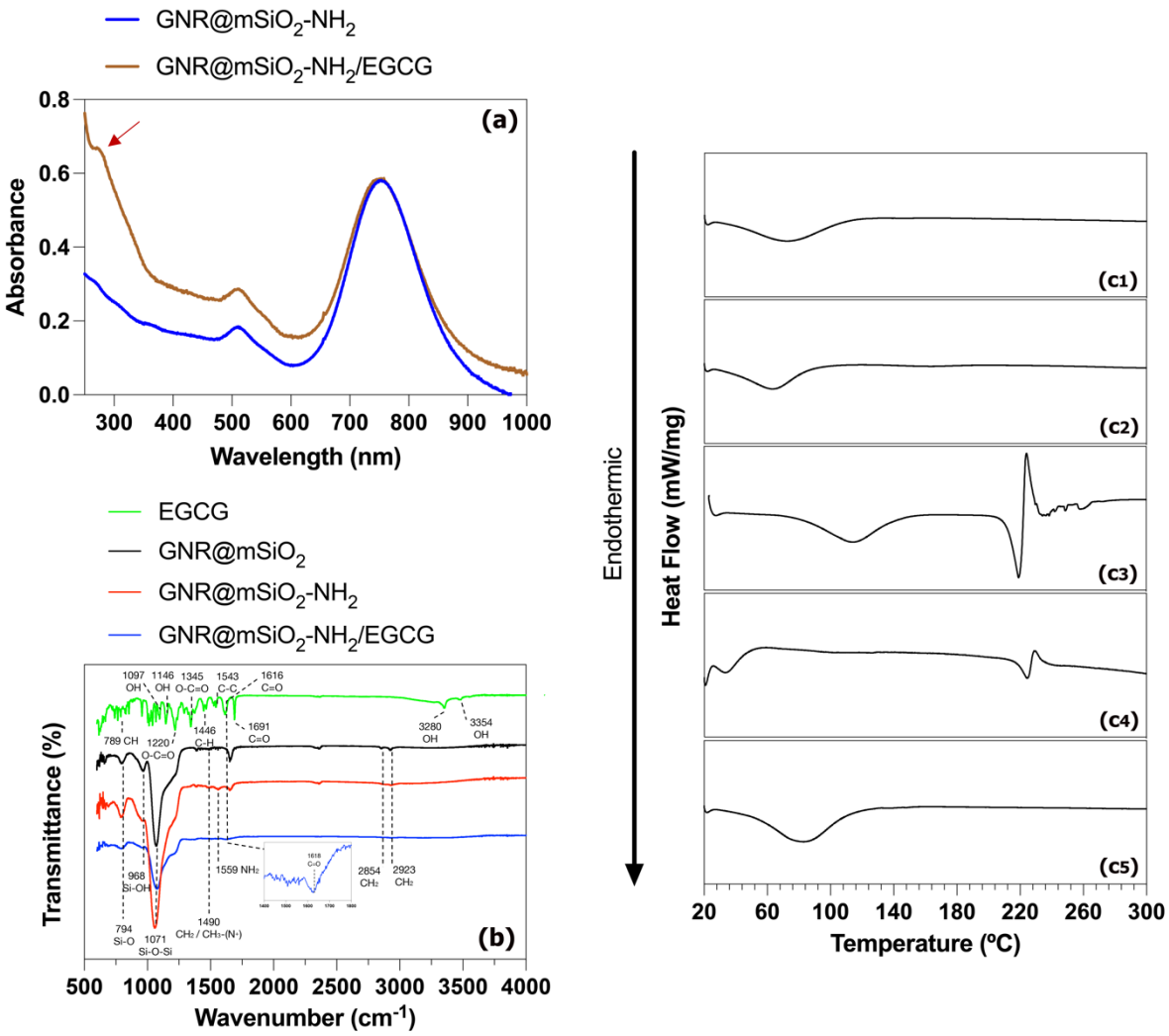

Figure 2: UV-Vis-NIR absorption spectra of GNR@mSiO$_2$-NH$_2$ and GNR@mSiO$_2$-NH$_2$/EGCG (a), FT-IR spectra of GNR@mSiO$_2$, GNR@mSiO$_2$-NH$_2$, GNR@mSiO$_2$-NH$_2$/EGCG and EGCG (b), and DSC curves of GNR@mSiO$_2$ (c$_1$), GNR@mSiO$_2$-NH$_2$ (c$_2$), EGCG (c$_3$), physical mixture GNR@mSiO$_2$-NH$_2$ + EGCG (c$_4$) and GNR@mSiO$_2$-NH$_2$/EGCG (c$_5$).

The thermogram of pure-EGCG shows (Figure 2c$_3$) a sharp endothermic peak at 219.3 ºC attributed to the melting point of EGCG. This endothermic peak demonstrates the crystalline nature of EGCG [62, 65-67]. The thermogram also shows a sharp exothermic peak at 224.2 °C, which is probably attributed to the decomposition of EGCG [65]. The thermogram of the physical mixture EGCG + GNR@mSiO$_2$-NH$_2$ (Figure 2c$_4$) showed a reduced intensity at the melting point of EGCG. The thermogram of GNR@mSiO$_2$-NH$_2$/EGCG (Figure 2c$_5$) reveals

the disappearance of the characteristic peaks of EGCG. This is presumably attributed to the transformation of the drug to an amorphous state upon adsorption onto the GNR@$mSiO_2$-NH_2. Other studies showed similar behavior of crystalline drugs loaded on a mesoporous silica surface [68, 69]. These observations suggest that EGCG was successfully incorporated into the mesoporous channels of GNR@$mSiO_2$-NH_2 in a non-crystalline form.

3.2. Adsorption isotherm

Any adsorption process usually is controlled by three diffusion steps, determining the kinetics of adsorption: (i) transport of the solute from the bulk solution to the film surrounding the adsorbent, (ii) from the film to the surface of the adsorbent, and (iii) from the surface to the internal sites of the particle [70]. Moreover, the adsorbed amount is mainly determined by energetic terms, such as (a) the physicochemical and structural characteristics of the molecule being absorbed (adsorbate) [71-73], (b) the type of medium in which diffusion and adsorption itself occurs [74], (c) the physicochemical and structural characteristics of the adsorbent particle [75-77], and (d) the type of interactions between the adsorbent and the adsorbate (determined by a, b and c) [78]. Figure 3a corresponds to the amount of EGCG adsorbed per amount of GNR@$mSiO_2$-NH_2 versus the initial amount of EGCG. It can be seen that the amount of EGCG adsorbed increased when the initial amount of EGCG increased, reaching saturation from initial values of 0.2 mg (initial EGCG/NPs ratio = 0.17; initial EGCG/$mSiO_2$ ratio = 0.44). The maximum adsorption of EGCG was 64.4 mg/g equivalent to a load of 6.0% and an encapsulation efficiency (EE) equal to 19.2%. If only the $mSiO_2$ shell is considered, which is equivalent to ≈ 40% w/w of the GNR@$mSiO_2$, the maximum adsorption of EGCG was 160.9 mg/g equivalent to a loading capacity of 13.9%. Hu et al. [79] reported that the maximum absorption of EGCG on mesoporous silica nanospheres (MSN) (diameter = 78 ± 5 nm, pore surface area = 557 m^2/g, pore volume = 0.93 cm^3/g, average pore size = 2.6 nm) was 276 mg/g (initial EGCG/NPs ratio = 0.8), i.e. 1.7 and 2.5 times higher than in the $mSiO_2$ layer of our amino-functionalized (160.9 mg/g) and non-amino-functionalized NPs (111.3 mg/g), respectively, even though the surface area of $mSiO_2$ of our GNR@$mSiO_2$ was 2.2 times larger than that in MSN. In addition, Ding et al. [80] reported an EE and loading capacity of EGCG on MSN (diameter ≈ 50 nm and average pore size = 2 nm) of 66% and 25%, respectively. This difference in adsorption levels

may be due to the different conditions used in the loading process: type of solvent, initial EGCG/mSiO_2 ratio [74], and the contact time between EGCG and NPs [40]. However, our adsorption results are comparable with those reported for other phenolic compounds (morin, rutin, and quercetin) [40, 77, 81] and other types of active molecules (vitamin E, doxorubicin, camptothecin, and AlPcS4) [27, 30, 57, 82, 83] on mesoporous silica NPs.

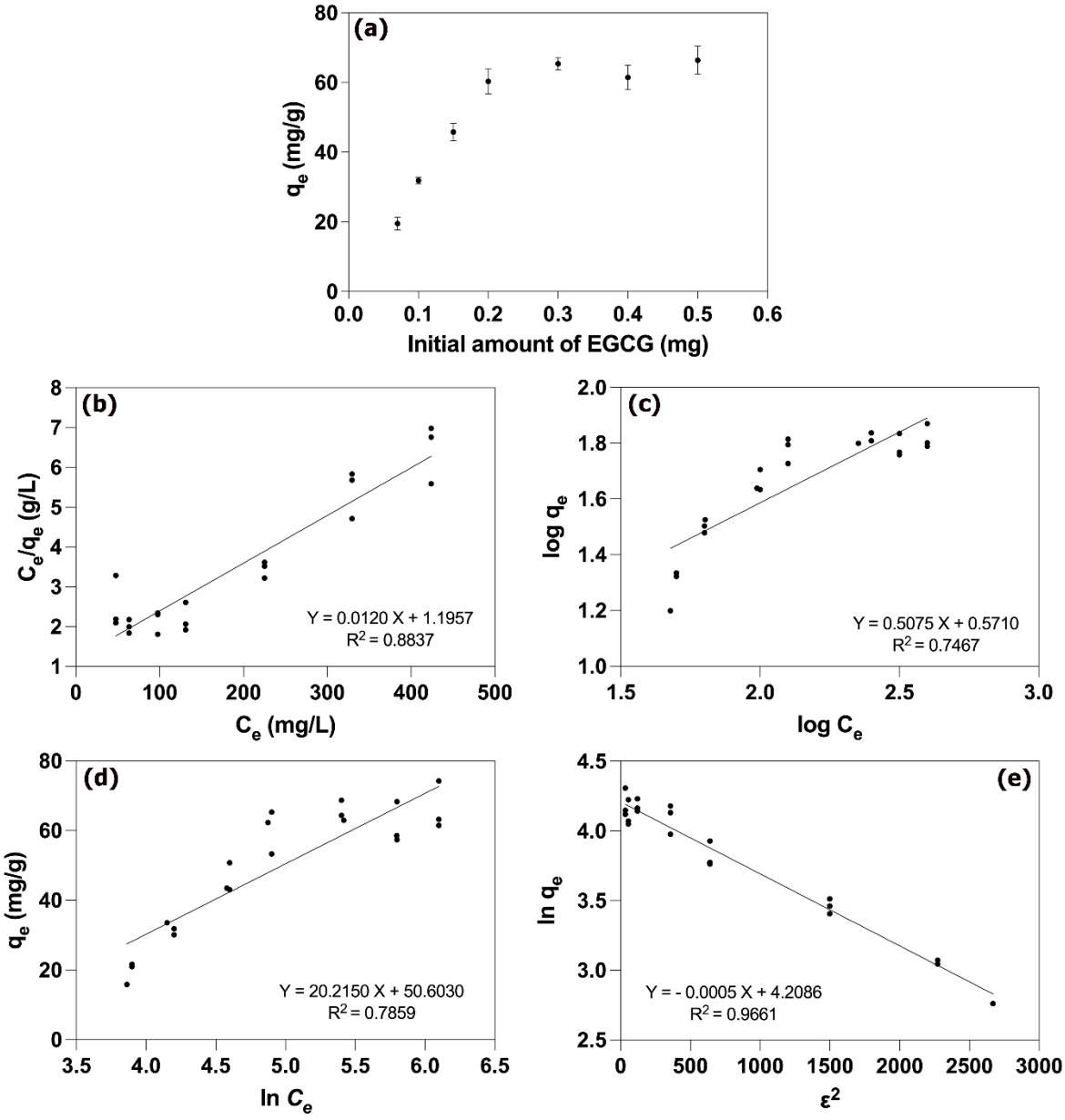

Figure 3: EGCG adsorption onto GNR@mSiO_2-NH_2. Adsorbed amount of EGCG as a function of different initial amount of EGCG (a); linear fit of experimental data obtained

using Langmuir (b), Freundlich (c), Temkin (d), and Dubinin-Radushkevich (e) isotherm models at 25 ºC (Mean ± SEM, n = 3).

It is clear that the type of functionalization together with the physicochemical and structural characteristics of the adsorbed molecule plays a fundamental role in the adsorption capacity [84]. According to other reports, the aminopropyl chains of the amino-functionalized nanosystem play an important role in the level of adsorption of molecules such as polyphenols [40, 77, 82], in particular through the establishment of van der Waals interactions [40]. It has been previously proposed that the adsorption of EGCG on an amino-functionalized surface occurs through two mechanisms: (i) formation of hydrogen bonds between the carbonyl and hydroxyl groups of EGCG and the amino groups, (ii) strong electrostatic interactions between the positively charged amino-functionalized surface and the negatively charged EGCG molecule (pKa = 7.7 [85]) [64]. This may explain the higher EE of EGCG in GNR@mSiO_2-NH_2 (≈ 1.5-fold) compared to GNR@mSiO_2 (data not shown).

Adsorption isotherms better express the magnitude of the retention and the behavior of the molecule on a solid surface once the equilibrium of the adsorption/desorption phenomena has been reached. They can be described from the ratio of the remaining concentration of a molecule to the concentration or amount of molecule retained on the solid surface at a constant temperature [86, 87].

The Langmuir, Freundlich, Temkin, and Dubinin-Radushkevich isotherm models are used to describe the adsorption equilibrium and provide information to elucidate the adsorption mechanism, surface properties, and the degree of affinity of the adsorbent for the adsorbate [40, 88, 89]. Consequently, we analyze our data according to the linearized forms of these adsorption isotherms whose equations are presented in Table 1.

Table 1: EGCG adsorption isotherm parameters in GNR@mSiO$_2$-NH$_2$.

Isotherm	Equation	Parameters
Langmuir	$\frac{C_e}{q_e} = \frac{1}{Q_m\, b} + \frac{1}{Q_m} C_e$ (**5**)	Q_m (mg/g) = 83.3
		b (L/mg) = 0.01
		R^2 = 0.8837
		R_L = 0.17 - 0.59
Freundlich	$\log(q_e) = \log K_f + \frac{1}{n} \log C_e$ (**6**)	K_f ((mg/g)(L/mg)$^{1/n}$) = 3.4
		n = 1.97
		R^2 = 0.7467
Temkin	$q_e = B \ln A + B \ln C_e$ (**7**)	B = 20.0
		A (L/mg) = 12.2
		R^2 = 0.7859
Dubinin-Radushkevich	$\ln q_e = \ln Q_s - K\varepsilon^2$ (**8**) $\varepsilon = RT \ln (1 + \frac{1}{C_e})$	Q_s = 67.3
		K × 10^{-7} (mol^2/kJ^2) = 0.0005
		E_a = 100.0
		R^2 = 0.9661

q_e = amount of EGCG adsorbed at equilibrium per unit of GNR@mSiO$_2$-NH$_2$ (mg/g), C_e = concentration of residual EGCG remaining in solution after adsorption (mg/L), Q_m = maximum monolayer absorption of EGCG per unit of GNR@mSiO$_2$-NH$_2$ (mg/g), b = Langmuir constant for adsorbate-adsorbent equilibrium (L/mg); K_f = Freundlich coefficient, n = is the Freundlich constant; A =Temkin isothermal constant (L/mg), B = constant defined as B = RT/b_T (T = absolute temperature in Kelvin, R = universal gas constant 8.3143 J/mol K, b_T = is a constant related to the heat of adsorption); Q_s = maximum absorption of EGCG per unit of GNR@mSiO$_2$-NH$_2$ (mg/g) [1, 2].

The Langmuir model considers a monolayer adsorption, that is, the adsorption would occur in a finite number of localized sites, without lateral interaction or steric hindrance between the adsorbed molecules. Under these conditions, maximum adsorption is reached when a saturated monolayer of molecules is produced on the solid surface [2, 87]. The Freundlich model assumes a non-ideal and reversible multilayer adsorption, applicable to heterogeneous surfaces with a non-uniform distribution of heat of adsorption and intensities of affinity on the surface [2, 87]. On the other hand, the Temkin model takes into account the indirect interactions between the adsorbent and adsorbate. This isotherm assumes that the heat of adsorption of all molecules in the layer decreases linearly with increasing coverage due to adsorbate-adsorbent interactions, thus adsorption is characterized by a uniform distribution of binding energies [1]. The Dubinin-Radushkevich isotherm model is an empirical model that presents information on the type of adsorption [1, 90].

According to the determination coefficients (R^2) (Table 1), the adsorption behavior of EGCG on the GNR@mSiO$_2$-NH$_2$ is better fitted by the Dubinin-Radushkevich model (R^2 = 0.9661)

compared to the rest of the studied models (Langmuir R^2 = 0.8837, Freundlich R^2 = 0.7467, and Temkin R^2 = 0.7859).

The Dubinin-Radushkevich adsorption model yields a maximum amount of EGCG adsorbed per amount of GNR@mSiO$_2$-NH$_2$ of 67.3 mg/g, a value very close to that obtained experimentally (64.4 mg/g). The adsorption activation energy (E_a), which is defined as the free energy change when one mole of molecules is transferred from the solution to the solid surface [2], was calculated from the isotherm of Dubinin-Radushkevich adsorption as follows:

$$E_a = \frac{1}{\sqrt{2K}} \qquad (\mathbf{9})$$

The magnitude of E_a gives information about the nature of the adsorption process. E_a values in the range of E_a in the range 1-8 kJ/mol correspond to a physical adsorption; between 9-16 kJ/mol is associated with ion exchange; and more than 16 kJ/mol represents a chemical adsorption [91]. The calculated E_a value was 100 kJ/mol at 25 ºC, which indicates that the adsorption of EGCG on GNR@mSiO$_2$-NH$_2$ corresponds to a strong chemical adsorption, compatible with electrostatic interactions between the surface OH and NH$_2$ groups and the phenol functions.

3.3. Kinetic Adsorption

The general rate of the adsorption process is determined by the slowest step, usually the diffusion of the solute from the surface film of the adsorbent to the internal sites of the particles [70].

Figure 4a shows the effect of the contact time between GNR@mSiO$_2$-NH$_2$ and EGCG, where a gradual adsorption process is observed during the first 6 h. After that, a second final equilibrium stage was observed where maximum adsorption was reached, probably due to a decrease in the number of available adsorption sites and the reduction in the concentration of EGCG in the solution [40].

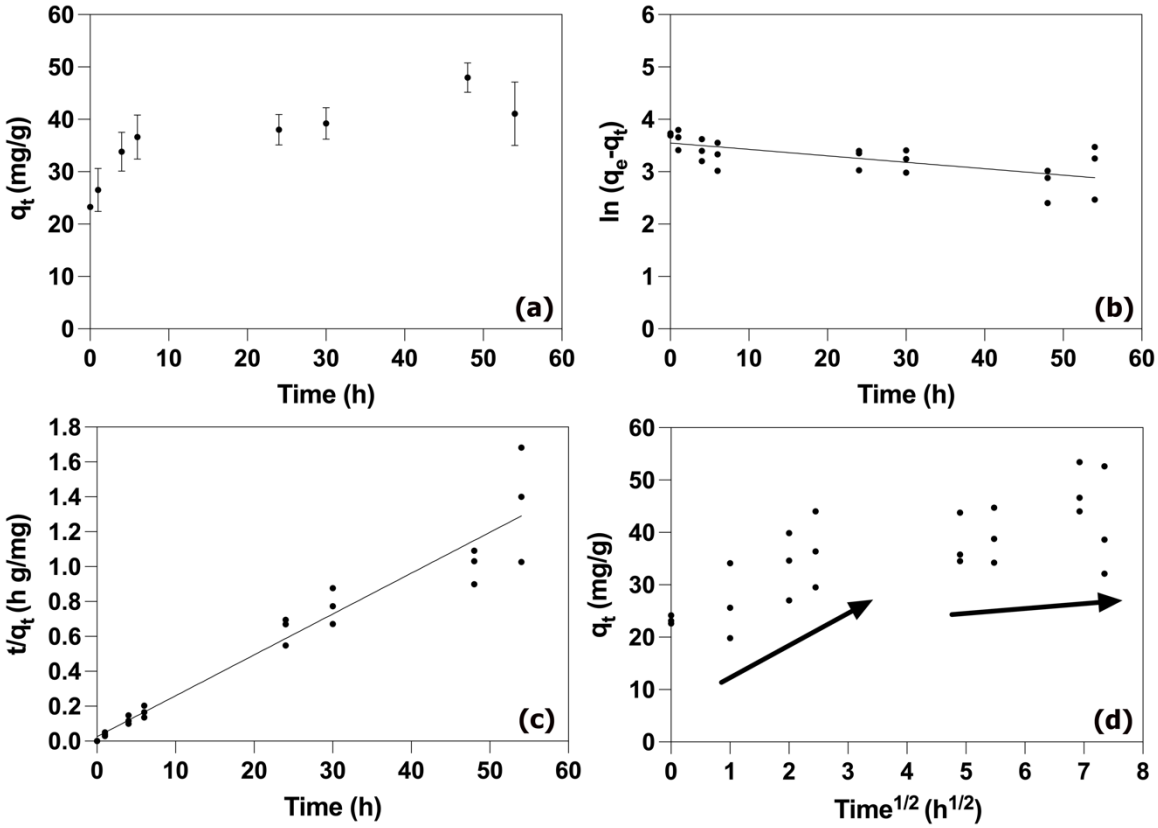

Figure 4: EGCG adsorption kinetics on GNR@mSiO$_2$-NH$_2$. Effect of contact time (Mean ± SEM, n = 3) (a), linear fit of experimental data obtained using pseudo-first order model (b), pseudo-second order model (c), and intra-particle diffusion model (d).

The adsorption kinetics of EGCG on GNR@mSiO$_2$-NH$_2$ was analyzed using three different kinetic models: the pseudo-first-order first proposed by Lagergren (Equation 9), the pseudo-second-order model of Ho and McKay (Equation 10), and the model of Weber and Morris intraparticle diffusion (Equation 11):

$$\ln(q_e - q_t) = \ln q_e - k_1 t \quad (\mathbf{9})$$

$$\frac{t}{q_t} = \frac{1}{k_2 {q_e}^2} + \frac{t}{q_e} \quad (\mathbf{10})$$

$$q_t = K_{id}\, t^{\frac{1}{2}} + I \quad (\mathbf{11})$$

Where q_e and q_t are the amounts of EGCG adsorbed on GNR@mSiO$_2$-NH$_2$ at equilibrium and at time t, respectively; k_1 is the observed rate constant of the pseudo-first-order model and k_2 is the observed rate constants of the pseudo-second-order model. K_{id} is the intraparticle diffusion rate constant and I is related to the thickness of the boundary layer.

As the results in Table 2 show, the coefficient of determination (R^2) values of the linear fits (Figure 4) suggest that the pseudo-second-order model is more suitable for predicting the kinetic mechanism for EGCG adsorption on GNR@mSiO$_2$-NH$_2$ in the present work. The value of q_e obtained with the pseudo-second-order model is close to the value obtained experimentally. Until now, no works have been published that describe the adsorption process of EGCG on silica NPs, however, other works on kinetic processes involving silica NPs agree that the pseudo-second-order model is the most adequate to predict the behavior of different compounds adsorbed on silica NPs [70, 92-94], including some phenolic compounds [40, 89].

Table 2: Kinetic parameters of EGCG absorption in GNR@mSiO$_2$-NH$_2$.

Kinetics model	Equation	Parameters
Pseudo first-order	$\ln(q_e - q_t) = -0.0123\,t + 3.5496$	k_1 (1/h) = 0.0123
		q_e (mg/g) = 34.8
		R^2 = 0.4667
Pseudo second-order	$\frac{t}{q_t} = 0.0234\,t + 0.0259$	k_2 = 0.0234
		q_e (mg/g) = 42.7
		R^2 = 0.9358
Intra-particle diffusion	$q_t = 5.6038\,t^{\frac{1}{2}} + 22.421$	K_{id1} (g/mg h$^{1/2}$) = 5.6038
		I_1 = 22.421
		R^2 = 0.5263
	$q_t = 2.5575\,t^{\frac{1}{2}} + 25.823$	K_{id2} (g/mg h$^{1/2}$) = 2.5575
		I_2 = 25.823
		R^2 = 0.1451

The steps of the adsorption process were thoroughly studied with the intraparticle diffusion model of Weber and Morris, as shown in Figure 4d. According to Equation 11, if the graph turns out to be a straight line, it can be concluded that intraparticle diffusion is the only step that controls the rate of adsorption. But as seen in Figure 4d, the adsorption data presents a multilinear plot, gradual adsorption followed by a final equilibrium stage of the process, suggesting that there is more than one step involved in the adsorption Process [40, 93]. The

results obtained suggest a complex adsorption process in which chemisorption, in addition to intraparticle diffusion, could be a rate-limiting step of adsorption [40].

3.4. Antioxidant activity evaluation

3.4.1. DPPH• assay

The DPPH• assay, which is based on the reduction of DPPH• to non-radial DPPH-H, is an easy-to-use, rapid, reproducible, and low-cost method for detecting the ability of compounds to scavenge free radicals [95, 96]. Furthermore, this assay has been widely used by several authors to evaluate the activity of polyphenols and other compounds incorporated in silica NPs [41, 77, 81, 82, 97-99]

Taking into account the results of this work, EGCG eliminates the DPPH• radical through a moderate kinetic pattern according to the classification proposed by Xie and Schaich [100], where it first acts by an electron transfer mechanism (SET) and, as the reaction proceeds, hydrogen atom transfer (HAT) appears. As shown in Figure 5a, for GNR@$mSiO_2$-NH_2/EGCG, an increase in EGCG concentration in the range of 0.05-1 µg/mL produced a rise in free radical scavenging activity, expressed as RSA. A comparison of the RSA of EGCG and GNR@$mSiO_2$-NH_2/EGCG showed that the antiradical activity was directly related to the amount of EGCG in the NPs. According to the results, attenuation in the scavenging activity of GNR@$mSiO_2$-NH_2/EGCG is observed compared to free EGCG in the range of 0.2-1 µg/mL. Other authors have also reported this phenomenon for polyphenols and other compounds incorporated in silica NPs [41, 77, 81, 82, 97-99]. It is believed that this behavior is due to the immobilization of the active molecules at the surface of the NPs and the tendency of DPPH• to be absorbed into the NPs; this causes a limitation to the free diffusion of the molecules involved, which hinders the antioxidant activity. However, the free radical scavenging activity of GNR@$mSiO_2$-NH_2/EGCG remains very high, reaching an RSA of 60.7 ± 6.9% at an EGCG equivalent concentration of 1 µg/mL, so the data suggests that the EGCG scaffold necessary to carry out the radical scavenging mechanism remains available after adsorption on GNR@$mSiO_2$-NH_2. As expected, GNR@$mSiO_2$-NH_2 alone did not show any significant effect against DPPH•. After 20 min of incubation at room temperature, only 2.9 ± 0.2% of the EGCG loaded in GNR@$mSiO_2$-NH_2 is desorbed (Figure S8a of the Supplementary Material), so the free radical-scavenging activity of GNR@$mSiO_2$-

NH_2/EGCG corresponds mainly to the action of EGCG adsorbed on the GNR@mSiO_2-NH_2 nanoparticles. For comparison, Arriagada et al. [41, 97] reported RSA of ~87% and ~95% for caffeic acid (17 µg/mL) and rosmarinic acid (10.8 µg/mL) immobilized on mesoporous silica NPs, respectively.

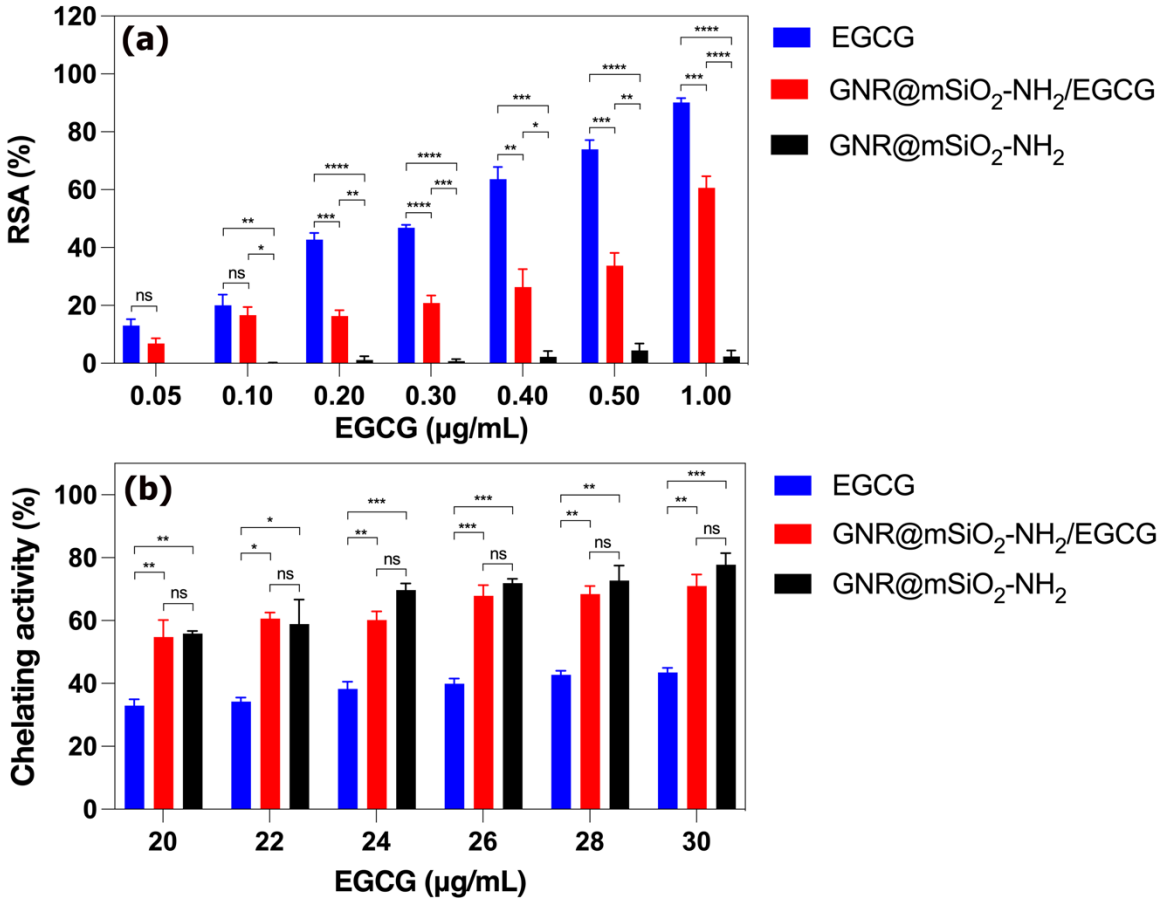

Figure 5: RSA (a) and chelating activity (b) of free EGCG, EGCG adsorbed on GNR@mSiO_2-NH_2, and GNR@mSiO_2-NH_2. Significance level: * $p < 0.05$, ** $p < 0.01$, *** $p < 0.001$, **** $p < 0.0001$ and ns: not significant ($p > 0.05$). Mean ± SEM, n = 3.

3.4.2. Chelating activity evaluation

Free or loosely bound Fe^{3+} (also Cu^{2+}) is an effective catalyst for the production of free radicals or reactive oxygen species (ROS), which can be reduced to Fe^{2+} by physiologically relevant reducing agents (such as glutathione or ascorbate) and can then react through the Fenton reaction with hydrogen peroxide (H_2O_2) to form hydroxyl radical (OH•), one of the

most reactive ROS [101-103]. Consequently, it is essential that an antioxidant nanosystem have a good metal chelation activity to avoid oxidative stress and damage.

The ability of NPs as metal chelators was studied, based on their ability to inhibit the formation of the Fe^{2+}-ferrozine complex. As depicted in Figure 5b, the chelating activity increases with the concentration of GNR@$mSiO_2$-NH_2/EGCG. The chelating activity of GNR@$mSiO_2$-NH_2/EGCG was statistically higher than that of free EGCG in the concentration range studied. However, the activity of GNR@$mSiO_2$-NH_2/EGCG was not statistically more elevated than that of GNR@$mSiO_2$-NH_2. Considering the low chelating activity of the GNR@$mSiO_2$ control (between 9 and 14%) (Figure S6 of the Supplementary Material) and what has been reported by other authors [41, 77], the chelating activity of GNR@$mSiO_2$-NH_2 is high thanks to the presence of free amino groups at the surface of the NPs. After 10 min of incubation at room temperature, only 5.8 ± 0.1% of the EGCG loaded into GNR@$mSiO_2$-NH_2 is desorbed (Figure S8b of the Supplementary Material), so the chelating activity of GNR@$mSiO_2$-NH_2/EGCG is mainly due to the action of adsorbed EGCG molecules and GNR@$mSiO_2$-NH_2 nanoparticles. The results of the FT-IR and adsorption isotherm analyses suggest that EGCG chemo-adsorbs to GNR@$mSiO_2$-NH_2 through the formation of hydrogen bonds between the hydroxyl and carbonyl groups of EGCG and the amino groups on the surface of the NPs, therefore the EGCG scaffold necessary to exert its chelating activity (hydroxyl groups on carbons 3` and 4` of ring B and 3`` and 4`` of ring D [9, 11, 104]) is not sufficiently available, therefore, EGCG loading is not able to further enhance the chelating activity of GNR@$mSiO_2$-NH_2.

3.5. Stability of GN@$mSiO_2$ and EGCG against NIR irradiation

To evaluate the stability of the nanosystem, aqueous suspensions of GNR and GNR@$mSiO_2$ (1 nM) were irradiated with NIR for 15 min. The morphology (Figure 6b) and the UV-Vis-NIR spectrum (Figure S9c of the Supplementary Material) of the GNR remained intact, however, ultrasmall gold NPs are observed in the HR-TEM images. When naked GNR are irradiated with NIR, very high temperatures are reached on their surface that can be transmitted a few nanometers in the medium. Therefore, this surface temperature is higher than the global temperature reached by the medium in which the NPs are found [105]. The temperature levels that are reached depend on the concentration of NPs and the irradiation

power density [105, 106]. Plasmonic heating by NIR irradiation sustained over time could have caused photocracking of the GNRs with the formation of ultrasmall gold NPs of various sizes (Figure 6b), as previously reported by Khanadeev et al. [107]. The formation of the silica layer on the surface of the GNR increases its photostability (because it partially limits the absorption and emission of energy in the form of heat [33, 83]) and avoids unwanted changes. However, under certain conditions (*e.g.*, high NIR laser power density and/or $mSiO_2$ thin film thickness < 24 nm) a small or large amount of ultrasmall gold NPs could be generated as a result of the destruction partial or total of the GNR [107], even photocracking of the $mSiO_2$ shell can occur [107, 108]. The morphology (Figure 6d) and UV-Vis-NIR spectrum (Figure S9d of the Supplementary Material) of the GNR@$mSiO_2$ appear intact, however, ultrasmall gold NPs could also be observed.

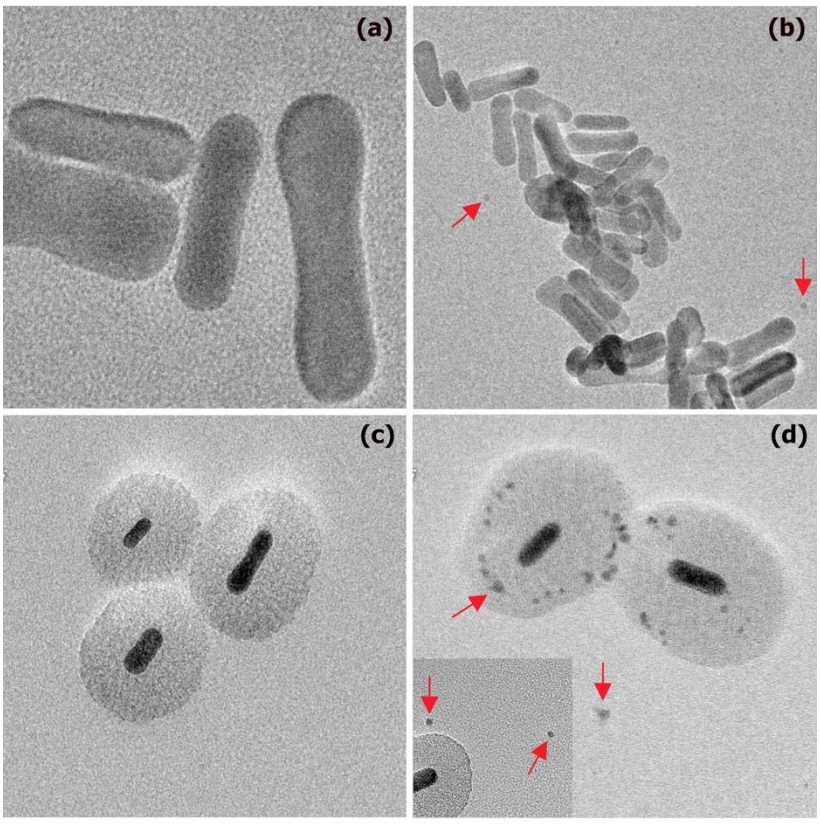

Figure 6: HR-TEM images of non-irradiated GNR (200000X) (a), NIR-irradiated GNR (60000X) (b), non-irradiated GNR@$mSiO_2$ (50000X) (c), and NIR-irradiated GNR@$mSiO_2$ (80000X) (d). Red arrows point to ultrasmall gold residues.

As detailed in Table S9 of the Supplementary Material, when NPs were irradiated with NIR, there was a slight increase in D_h that was not significant. Furthermore, an increase in PDI and a decrease in ZP were observed. This indicates that NIR irradiation may have favored the appearance of slightly more aggregates.

The core-shell nanosystem corresponding to GNR coated with $mSiO_2$ can be irradiated with NIR to stimulate and control the release of drugs adsorbed on the $mSiO_2$ coating through the photothermal effect [32]. According to the above, it is necessary to evaluate the stability of the drug to be nanovehiculized against NIR irradiation and temperature.

To evaluate the stability of EGCG, aqueous solutions were subjected to NIR irradiation, temperature bath, and both conditions simultaneously (NIR irradiation and temperature). According to Figure S10a of the Supplementary Material, EGCG remained stable against NIR irradiation, conserving 101.1 ± 6.5% of the concentration after 30 min.

When aqueous suspensions of GNR@$mSiO_2$ (3 nM) were subjected to NIR irradiation a maximum temperature of approximately 41°C was reached (Figure S9b of the Supplementary Material). This is an adequate temperature to stimulate the release of drugs adsorbed in this type of nanosystems [32] and, in addition, it is the maximum temperature that can be reached *in vivo* without causing cell apoptosis due to hyperthermia [109]. As observed in Figure S10b of the Supplementary Material, EGCG remained stable at 41 ºC, conserving 103.5 ± 3.7% of the concentration after 30 min. Similarly, EGCG remained stable when subjected to a temperature of 41ºC and NIR irradiation simultaneously, conserving 101.5 ± 6.2% of the concentration after 30 min (Figure S10C of the Supplementary Material). None of the stability tests observed the appearance of an additional signal in the chromatograms that could be interpreted as a degradation product (Figure S11 of the Supplementary Material).

Furthermore, the DPPH• radical inactivating ability and EGCG chelating activity were maintained after being exposed to NIR irradiation, temperature bath (41°C), and both conditions simultaneously (Figure S7 of the Supplementary Material). This confirms that the EGCG remains stable and functional after being exposed to the aforementioned conditions.

4. Conclusions

The objective of this work was to synthesize core-shell NPs composed of GNR@$mSiO_2$-NH_2 loaded with EGCG as a useful antioxidant material and to study their photothermal stability for their potential use in the chemo-photothermal therapy. Epigallocatechin-3-gallate is chemo-adsorbed on GNR@$mSiO_2$-NH_2, reaching loading capacity comparable to other reports related to the adsorption of phenolic compounds on mesoporous silica surfaces. The GNR@$mSiO_2$-NH_2/EGCG nanosystem presented good antioxidant activity evaluated in terms of its RSA and chelating activity. EGCG, as well as its antioxidant activity (RSA and chelating activity), remained stable under NIR irradiation, at the temperature, and under both conditions simultaneously. In addition, the morphology and the UV-Vis-NIR spectrum of the NPs remained intact after being irradiated with NIR, although ultrasmall gold NPs could be observed, probably the product of photocracking of the GNR. According to these results, the GNR@$mSiO_2$-NH_2/EGCG nanosystem is potentially useful for the chemo-photothermal therapy.

Declaration of interests

The authors declare that they have no interests that may have influenced the work reported in this document.

Acknowledgments

This work was supported by the National Fund for Scientific and Technological Development (FONDECYT) [Projects 1221145 and 1211482]. Javier Avendaño-Godoy is grateful to ANID/Scholarship Program/NATIONAL DOCTORATE/2020-21202096 and Ministère de l'Europe et des Affaires-Campus France/EIFFEL EXCELLENCE SCHOLARSHIP/116702Q (2022-2023).

References

[1] N. Ayawei, A.N. Ebelegi, D. Wankasi, Modelling and interpretation of adsorption isotherms, J Chem, 2017 (2017) 1-11.

[2] K.Y. Foo, B.H. Hameed, Insights into the modeling of adsorption isotherm systems, Chem Eng J, 156 (2010) 2-10.

[3] H.S. Kim, M.J. Quon, J.A. Kim, New insights into the mechanisms of polyphenols beyond antioxidant properties; lessons from the green tea polyphenol, epigallocatechin 3-gallate, Redox Biol, 2 (2014) 187-195.

[4] L. Chen, H.-Y. Zhang, Cancer Preventive Mechanismsof the Green Tea Polyphenol (-)-Epigallocatechin-3-gallate, Molecules, 12 (2007) 946-957.

[5] Y.-Q. Xu, P. Yu, W. Zhou, Combined effect of pH and temperature on the stability and antioxidant capacity of epigallocatechin gallate (EGCG) in aqueous system, J Food Eng, 250 (2019) 46-54.

[6] P.T. Devika, P. Stanely Mainzen Prince, (-)Epigallocatechin-gallate (EGCG) prevents mitochondrial damage in isoproterenol-induced cardiac toxicity in albino Wistar rats: a transmission electron microscopic and in vitro study, Pharmacol Res, 57 (2008) 351-357.

[7] M. Perusko, A. Al-Hanish, J. Mihailovic, S. Minic, S. Trifunovic, I. Prodic, T. Cirkovic Velickovic, Antioxidative capacity and binding affinity of the complex of green tea catechin and beta-lactoglobulin glycated by the Maillard reaction, Food Chem, 232 (2017) 744-752.

[8] K. Nilsuwan, S. Benjakul, T. Prodpran, Properties and antioxidative activity of fish gelatin-based film incorporated with epigallocatechin gallate, Food Hydrocoll, 80 (2018) 212-221.

[9] S.L. Sun, G.Q. He, H.N. Yu, J.G. Yang, D. Borthakur, L.C. Zhang, S.R. Shen, U.N. Das, Free Zn(2+) enhances inhibitory effects of EGCG on the growth of PC-3 cells, Mol Nutr Food Res, 52 (2008) 465-471.

[10] K.F. Pirker, M.C. Baratto, R. Basosi, B.A. Goodman, Influence of pH on the speciation of copper(II) in reactions with the green tea polyphenols, epigallocatechin gallate and gallic acid, J Inorg Biochem, 112 (2012) 10-16.

[11] P. Ryan, M.J. Hynes, The kinetics and mechanisms of the complex formation and antioxidant behaviour of the polyphenols EGCg and ECG with iron(III), J Inorg Biochem, 101 (2007) 585-593.

[12] Y. Zhong, C.M. Ma, F. Shahidi, Antioxidant and antiviral activities of lipophilic epigallocatechin gallate (EGCG) derivatives, J Funct Foods, 4 (2012) 87-93.

[13] S.K. Sonawane, H. Chidambaram, D. Boral, N.V. Gorantla, A.A. Balmik, A. Dangi, S. Ramasamy, U.K. Marelli, S. Chinnathambi, EGCG impedes human Tau aggregation and interacts with Tau, Sci Rep, 10 (2020) 12579.

[14] H.J. Wobst, A. Sharma, M.I. Diamond, E.E. Wanker, J. Bieschke, The green tea polyphenol (-)-epigallocatechin gallate prevents the aggregation of tau protein into toxic oligomers at substoichiometric ratios, FEBS Lett, 589 (2015) 77-83.

[15] J. Bieschke, J. Russ, R.P. Friedrich, D.E. Ehrnhoefer, H. Wobst, K. Neugebauer, E.E. Wanker, EGCG remodels mature alpha-synuclein and amyloid-beta fibrils and reduces cellular toxicity, PNAS, 107 (2010) 7710-7715.

[16] S.J. Hyung, A.S. DeToma, J.R. Brender, S. Lee, S. Vivekanandan, A. Kochi, J.S. Choi, A. Ramamoorthy, B.T. Ruotolo, M.H. Lim, Insights into antiamyloidogenic properties of the green tea extract (-)-epigallocatechin-3-gallate toward metal-associated amyloid-beta species, PNAS, 110 (2013) 3743-3748.

[17] S. Zhang, Q. Zhu, J.Y. Chen, D. OuYang, J.H. Lu, The pharmacological activity of epigallocatechin-3-gallate (EGCG) on Alzheimer's disease animal model: A systematic review, Phytomedicine, 79 (2020) 153316.
[18] A.P. Neilson, A.S. Hopf, B.R. Cooper, M.A. Pereira, J.A. Bomser, M.G. Ferruzzi, Catechin degradation with concurrent formation of homo- and heterocatechin dimers during in vitro digestion, J Agric Food Chem, 55 (2007) 8941-8949.
[19] L. Zhang, Y. Zheng, M.S. Chow, Z. Zuo, Investigation of intestinal absorption and disposition of green tea catechins by Caco-2 monolayer model, Int J Pharm, 287 (2004) 1-12.
[20] L.-C. Lin, M.-N. Wang, T.-Y. Tseng, Sung, T.-H. Tsai, Pharmacokinetics of (−)-epigallocatechin-3-gallate in conscious and freely moving rats and its brain regional distribution, J Agric Food Chem, 55 (2007) 1517-1524.
[21] A. Takagaki, F. Nanjo, Metabolism of (-)-epigallocatechin gallate by rat intestinal flora, J Agric Food Chem, 58 (2010) 1313-1321.
[22] M. Pervin, K. Unno, A. Nakagawa, Y. Takahashi, K. Iguchi, H. Yamamoto, M. Hoshino, A. Hara, A. Takagaki, F. Nanjo, A. Minami, S. Imai, Y. Nakamura, Blood brain barrier permeability of (-)-epigallocatechin gallate, its proliferation-enhancing activity of human neuroblastoma SH-SY5Y cells, and its preventive effect on age-related cognitive dysfunction in mice, Biochem Biophys Rep, 9 (2017) 180-186.
[23] R. Kumar, K. Mondal, P.K. Panda, A. Kaushik, R. Abolhassani, R. Ahuja, H.-G. Rubahn, Y.K. Mishra, Core–shell nanostructures: perspectives towards drug delivery applications, J Mater Chem B, 8 (2020) 8992-9027.
[24] H. Zhou, H. Xu, X. Li, Y. Lv, T. Ma, S. Guo, Z. Huang, X. Wang, P. Xu, Dual targeting hyaluronic acid - RGD mesoporous silica coated gold nanorods for chemo-photothermal cancer therapy, Mater Sci Eng C, 81 (2017) 261-270.
[25] H. Guo, S. Yi, K. Feng, Y. Xia, X. Qu, F. Wan, L. Chen, C. Zhang, In situ formation of metal organic framework onto gold nanorods/mesoporous silica with functional integration for targeted theranostics, Chem Eng Sci, 403 (2021).
[26] C. Li, K. Feng, N. Xie, W. Zhao, L. Ye, B. Chen, C.-H. Tung, L.-Z. Wu, Mesoporous silica-coated gold nanorods with designable anchor peptides for chemo-photothermal cancer therapy, ACS Appl Nano Mater 3(2020) 5070-5078.
[27] X. Yang, Z. Liu, Z. Li, F. Pu, J. Ren, X. Qu, Near-infrared-controlled, targeted hydrophobic drug-delivery system for synergistic cancer therapy, Chemistry, 19 (2013) 10388-10394.
[28] A.R. Guerrero, N. Hassan, C.A. Escobar, F. Albericio, M.J. Kogan, E. Araya, Gold nanoparticles for photothermally controlled drug release, Nanomedicine 9(2014) 2023-2039.
[29] C. Adura, S. Guerrero, E. Salas, L. Medel, A. Riveros, J. Mena, J. Arbiol, F. Albericio, E. Giralt, M.J. Kogan, Stable conjugates of peptides with gold nanorods for biomedical applications with reduced effects on cell viability, ACS Appl Mater Interfaces, 5 (2013) 4076-4085.
[30] S. Shen, H. Tang, X. Zhang, J. Ren, Z. Pang, D. Wang, H. Gao, Y. Qian, X. Jiang, W. Yang, Targeting mesoporous silica-encapsulated gold nanorods for chemo-photothermal therapy with near-infrared radiation, Biomaterials, 34 (2013) 3150-3158.
[31] Z. Song, J. Shi, Z. Zhang, Z. Qi, S. Han, S. Cao, Mesoporous silica-coated gold nanorods with a thermally responsive polymeric cap for near-infrared-activated drug delivery, J Mater Sci, 53 (2018) 7165-7179.

[32] Z. Zhang, L. Wang, J. Wang, X. Jiang, X. Li, Z. Hu, Y. Ji, X. Wu, C. Chen, Mesoporous silica-coated gold nanorods as a light-mediated multifunctional theranostic platform for cancer treatment, Adv Mater, 24 (2012) 1418-1423.
[33] J. Wang, W. Zhang, S. Li, D. Miao, G. Qian, G. Su, Engineering of porous silica coated gold nanorods by surface-protected etching and their applications in drug loading and combined cancer therapy, Langmuir, 35 (2019) 14238-14247.
[34] N.T. Ha Lien, A.D. Phan, B.T. Van Khanh, N.T. Thuy, N. Trong Nghia, H.T. My Nhung, T. Hong Nhung, D. Quang Hoa, V. Duong, N. Minh Hue, Applications of mesoporous silica-encapsulated gold nanorods loaded doxorubicin in chemo-photothermal therapy, ACS Omega, 5 (2020) 20231-20237.
[35] P. Jara-Guajardo, P. Cabrera, F. Celis, M. Soler, I. Berlanga, N. Parra-Munoz, G. Acosta, F. Albericio, F. Guzman, M. Campos, A. Alvarez, F. Morales-Zavala, M.J. Kogan, Gold nanoparticles mediate improved detection of beta-amyloid aggregates by fluorescence, Nanomaterials, 10 (2020) 690.
[36] B. Nikoobakht, M.A. El-Sayed, Preparation and growth mechanism of gold nanorods (NRs) using seed-mediated growth method, Chem Mater, 15 (2003) 1957-1962.
[37] N.S. Abadeer, M.R. Brennan, W.L. Wilson, C.J. Murphy, Distance and plasmon wavelength dependent fluorescence of molecules bound to silica-coated gold nanorods, ACS Nano, 8 (2014) 8392-8406.
[38] S. Bhattacharjee, DLS and zeta potential – What they are and what they are not?, J Control Release, 235 (2016) 337-351.
[39] ICH, ICH Harmonised tripartite guideline validation of analytical procedures: text and methodology Q2 (R1), (2005).
[40] F. Arriagada, O. Correa, G. Gunther, S. Nonell, F. Mura, C. Olea-Azar, J. Morales, Morin flavonoid adsorbed on mesoporous silica, a novel antioxidant nanomaterial, PLoS One, 11 (2016) e0164507.
[41] F. Arriagada, G. Gunther, J. Nos, S. Nonell, C. Olea-Azar, J. Morales, Antioxidant nanomaterial based on core(-)shell silica nanospheres with surface-bound caffeic acid: A promising vehicle for oxidation-sensitive drugs, Nanomaterials (Basel), 9 (2019).
[42] S. Yoon, B. Lee, C. Kim, J.H. Lee, Controlled heterogeneous nucleation for synthesis of uniform mesoporous silica-coated gold nanorods with tailorable rotational diffusion and 1 nm-scale size tunability, Cryst Growth Des, 18 (2018) 4731-4736.
[43] X. Cattoën, S. Kodjikian, P. Trens, Periodic mesoporous organosilica nanoparticles: Morphology control and sorption properties, Colloids Surf A: Physicochem Eng Asp, 677 (2023).
[44] Y. Yu, M. Zhou, W. Zhang, L. Huang, D. Miao, H. Zhu, G. Su, Rattle-type gold danorods/porous-SiO2 nanocomposites as near-infrared light-activated drug delivery systems for cancer combined chemo-photothermal therapy, Mol Pharmaceutics, 16 (2019) 1929-1938.
[45] Z. Song, Y. Liu, J. Shi, T. Ma, Z. Zhang, H. Ma, S. Cao, Hydroxyapatite/mesoporous silica coated gold nanorods with improved degradability as a multi-responsive drug delivery platform, Mater Sci Eng C Mater Biol Appl, 83 (2018) 90-98.
[46] X. Cui, W. Cheng, X. Han, Lipid bilayer modified gold nanorod@mesoporous silica nanoparticles for controlled drug delivery triggered by near-infrared light, J Mater Chem B, 6 (2018) 8078-8084.
[47] C. Xu, F. Chen, H.F. Valdovinos, D. Jiang, S. Goel, B. Yu, H. Sun, T.E. Barnhart, J.J. Moon, W. Cai, Bacteria-like mesoporous silica-coated gold nanorods for positron emission

tomography and photoacoustic imaging-guided chemo-photothermal combined therapy, Biomaterials, 165 (2018) 56-65.
[48] Y. Liu, M. Xu, Q. Chen, G. Guan, W. Hu, X. Zhao, M. Qiao, H. Hu, Y. Liang, H. Zhu, D. Chen, Gold nanorods/mesoporous silica-based nanocomposite as theranostic agents for targeting near-infrared imaging and photothermal therapy induced with laser, Int J Nanomedicine, 10 (2015) 4747-4761.
[49] C. Hung, H. Bai, M. Karthik, Ordered mesoporous silica particles and Si-MCM-41 for the adsorption of acetone: A comparative study, Sep Purif Technol, 64 (2009) 265-272.
[50] Y. Zhang, H. Yan, J. Tang, P. Li, R. Su, H. Zhong, W. Su, Dual-mode antibacterial core-shell gold nanorod@mesoporous-silica/curcumin nanocomplexes for efficient photothermal and photodynamic therapy, J Photochem Photobiol A: Chem, 425 (2022).
[51] C.J. Orendorff, C.J. Murphy, Quantitation of Metal Content in the Silver-Assisted Growth of Gold Nanorods, J Phys Chem B, 110 (2006) 3990-3994.
[52] S.K. Filippov, R. Khusnutdinov, A. Murmiliuk, W. Inam, L.Y. Zakharova, H. Zhang, V.V. Khutoryanskiy, Dynamic light scattering and transmission electron microscopy in drug delivery: a roadmap for correct characterization of nanoparticles and interpretation of results, Mater Horiz, 10 (2023) 5354-5370.
[53] D.R. Dias, A.F. Moreira, I.J. Correia, The effect of the shape of gold core-mesoporous silica shell nanoparticles on the cellular behavior and tumor spheroid penetration, J Mater Chem B, 4 (2016) 7630-7640.
[54] J.L. Montaño-Priede, J.P. Coelho, A. Guerrero-Martínez, O. Peña-Rodríguez, U. Pal, Fabrication of Monodispersed Au@SiO2 Nanoparticles with Highly Stable Silica Layers by Ultrasound-Assisted Stöber Method, J Phys Chem C, 121 (2017) 9543-9551.
[55] J. Feng, Z. Wang, B. Shen, L. Zhang, X. Yang, N. He, Effects of template removal on both morphology of mesoporous silica-coated gold nanorod and its biomedical application, RSC Advances, 4 (2014) 28683-28690.
[56] A. Khanal, C. Ullum, C.W. Kimbrough, N.C. Garbett, J.A. Burlison, M.W. McNally, P. Chuong, A.S. El-Baz, J.B. Jasinski, L.R. McNally, Tumor targeted mesoporous silica-coated gold nanorods facilitate detection of pancreatic tumors using Multispectral optoacoustic tomography, Nano Res, 8 (2015) 3864-3877.
[57] G.-F. Luo, W.-H. Chen, Q. Lei, W.-X. Qiu, Y.-X. Liu, Y.-J. Cheng, X.-Z. Zhang, A triple-collaborative strategy for high-performance tumor therapy by multifunctional mesoporous silica-coated gold nanorods, Adv Funct Mater, 26 (2016) 4339-4350.
[58] S. Dahiya, R. Rani, D. Dhingra, S. Kumar, N. Dilbaghi, Conjugation of epigallocatechin gallate and piperine into a zein nanocarrier: Implication on antioxidant and anticancer potential, Adv Nat Sci Nanosci Nanotechnol, 9 (2018) 035011.
[59] S. Dahiya, R. Rani, S. Kumar, D. Dhingra, N. Dilbaghi, Chitosan-gellan gum bipolymeric nanohydrogels—a potential nanocarrier for the delivery of epigallocatechin gallate, BioNanoScience, 7 (2017) 508-520.
[60] R. Liu, X. Yan, Z. Liu, D.J. McClements, F. Liu, X. Liu, Fabrication and characterization of functional protein-polysaccharide-polyphenol complexes assembled from lactoferrin, hyaluronic acid and (-)-epigallocatechin gallate, Food Funct, 10 (2019) 1098-1108.
[61] V.S.S. Gonçalves, J. Poejo, A.A. Matias, S. Rodríguez-Rojo, M.J. Cocero, C.M.M. Duarte, Using different natural origin carriers for development of epigallocatechin gallate (EGCG) solid formulations with improved antioxidant activity by PGSS-drying, RSC Advances, 6 (2016) 67599-67609.

[62] R. Radhakrishnan, H. Kulhari, D. Pooja, S. Gudem, S. Bhargava, R. Shukla, R. Sistla, Encapsulation of biophenolic phytochemical EGCG within lipid nanoparticles enhances its stability and cytotoxicity against cancer, Chem Phys Lipids, 198 (2016) 51-60.
[63] F. Ke, M. Zhang, N. Qin, G. Zhao, J. Chu, X. Wan, Synergistic antioxidant activity and anticancer effect of green tea catechin stabilized on nanoscale cyclodextrin-based metal–organic frameworks, J Mater Sci, 54 (2019) 10420-10429.
[64] G. Ma, J. Zhang, L. Chen, T. Liu, L. Yu, X. Liu, C. Lu, Amino-functionalized ordered mesoporous silica SBA-15, a rapid and efficient adsorbent for the adsorption of (−)-epigallocatechin gallate from green tea extract, RSC Adv, 4 (2014) 41341-41347.
[65] M.A. Safwat, B.A. Kandil, M.A. Elblbesy, G.M. Soliman, N.E. Eleraky, Epigallocatechin-3-gallate-loaded gold nanoparticles: Preparation and evaluation of anticancer efficacy in ehrlich Tumor-bearing mice, Pharmaceuticals, 13 (2020).
[66] W. Fang, Z.L. Peng, Y.J. Dai, D.L. Wang, P. Huang, H.P. Huang, (-)-Epigallocatechin-3-gallate encapsulated realgar nanoparticles exhibit enhanced anticancer therapeutic efficacy against acute promyelocytic leukemia, Drug Deliv, 26 (2019) 1058-1067.
[67] K.S. Avadhani, J. Manikkath, M. Tiwari, M. Chandrasekhar, A. Godavarthi, S.M. Vidya, R.C. Hariharapura, G. Kalthur, N. Udupa, S. Mutalik, Skin delivery of epigallocatechin-3-gallate (EGCG) and hyaluronic acid loaded nano-transfersomes for antioxidant and anti-aging effects in UV radiation induced skin damage, Drug Deliv, 24 (2017) 61-74.
[68] T. Christoforidou, D. Giasafaki, E.G. Andriotis, N. Bouropoulos, N.F. Theodoroula, I.S. Vizirianakis, T. Steriotis, G. Charalambopoulou, D.G. Fatouros, Oral drug delivery systems based on ordered mesoporous silica nanoparticles for modulating the release of aprepitant, Int J Mol Sci, 22 (2021).
[69] Y. Lv, J. Li, H. Chen, Y. Bai, L. Zhang, Glycyrrhetinic acid-functionalized mesoporous silica nanoparticles as hepatocellular carcinoma-targeted drug carrier, Int J Nanomedicine, 12 (2017) 4361-4370.
[70] M. Anbia, S. Salehi, Removal of acid dyes from aqueous media by adsorption onto amino-functionalized nanoporous silica SBA-3, Dyes Pigm, 94 (2012) 1-9.
[71] C.M. Simonescu, D.C. Culita, A. Tatarus, T. Mocanu, G. Marinescu, R.A. Mitran, I. Atkinson, A. Kuncser, N. Stanica, Novel magnetic nanocomposites based on carboxyl-functionalized SBA-15 silica for effective dye adsorption from aqueous solutions, Nanomaterials (Basel), 12 (2022).
[72] L. Zauska, E. Benova, M. Urbanova, J. Brus, V. Zelenak, V. Hornebecq, M. Almasi, Adsorption and release properties of drug delivery system naproxen-SBA-15: Effect of surface polarity, sodium/acid drug form and pH, J Funct Biomater, 13 (2022).
[73] H. Ritter, J.H. Ramm, D. Bruhwiler, Influence of the structural properties of mesoporous silica on the adsorption of guest molecules, Materials (Basel), 3 (2010) 4500-4509.
[74] Y. He, S. Liang, M. Long, H. Xu, Mesoporous silica nanoparticles as potential carriers for enhanced drug solubility of paclitaxel, Mater Sci Eng C Mater Biol Appl, 78 (2017) 12-17.
[75] R. Wang, Y. Zhang, S. Gu, J. Shen, X. Wang, Y. He, Rational synthesis of monodisperse hollow mesoporous silica nanospheres for selective adsorption, ChemistrySelect, 8 (2023).
[76] S. Luo, J. Hao, Y. Gao, D. Liu, Q. Cai, X. Yang, Pore size effect on adsorption and release of metoprolol tartrate in mesoporous silica: Experimental and molecular simulation studies, Mater Sci Eng C Mater Biol Appl, 100 (2019) 789-797.

964 [77] G. Berlier, L. Gastaldi, S. Sapino, I. Miletto, E. Bottinelli, D. Chirio, E. Ugazio, MCM-
965 41 as a useful vector for rutin topical formulations: Synthesis, characterization and testing,
966 Int J Pharm, 457 (2013) 177-186.
967 [78] J.K. Kang, H. Lee, S.B. Kim, H. Bae, Alkyl chain length of quaternized SBA-15 and
968 solution conditions determine hydrophobic and electrostatic interactions for carbamazepine
969 adsorption, Sci Rep, 13 (2023) 5170.
970 [79] J. Hu, R. Xu, J. Hu, W. Deng, Dual stabilization of Pickering emulsion with
971 epigallocatechin gallate loaded mesoporous silica nanoparticles, Food Chem, 396 (2022)
972 133675.
973 [80] J. Ding, X. Kong, J. Yao, J. Wang, X. Cheng, B. Tang, Z. He, Core–shell mesoporous
974 silica nanoparticles improve HeLa cell growth and proliferation inhibition by (−)-
975 epigallocatechin-3-gallate by prolonging the half-life, J Mater Chem B, 22 (2012).
976 [81] D.M. Schlipf, C.A. Jones, M.E. Armbruster, E.S. Rushing, K.C. Wooten, S.E. Rankin,
977 B.L. Knutson, Flavonoid adsorption and stability on titania-functionalized silica
978 nanoparticles, Colloids Surf A Physicochem Eng Asp, 478 (2015) 15-21.
979 [82] Z. Mai, J. Chen, Y. Hu, F. Liu, B. Fu, H. Zhang, X. Dong, W. Huang, W. Zhou, Novel
980 functional mesoporous silica nanoparticles loaded with Vitamin E acetate as smart platforms
981 for pH responsive delivery with high bioactivity, J Colloid Interface Sci, 508 (2017) 184-
982 195.
983 [83] T. Zhang, Z. Ding, H. Lin, L. Cui, C. Yang, X. Li, H. Niu, N. An, R. Tong, F. Qu, pH-
984 Sensitive gold nanorods with a Mesoporous silica shell for drug release and photothermal
985 therapy, Eur J Inorg Chem, 2015 (2015) 2277-2284.
986 [84] H. Li, X. Chen, D. Shen, F. Wu, R. Pleixats, J. Pan, Functionalized silica nanoparticles:
987 classification, synthetic approaches and recent advances in adsorption applications,
988 Nanoscale, 13 (2021) 15998-16016.
989 [85] M. Muzolf, H. Szymusiak, A. Gliszczyńska-Świgło, I.M.C.M. Rietjens, B.e.
990 Tyrakowska, pH-Dependent radical scavenging capacity of green tea catechins, J Agric Food
991 Chem, 56 (2008) 816-823.
992 [86] M. Mozaffari Majd, V. Kordzadeh-Kermani, V. Ghalandari, A. Askari, M. Sillanpaa,
993 Adsorption isotherm models: A comprehensive and systematic review (2010-2020), Sci
994 Total Environ, 812 (2022) 151334.
995 [87] M.A. Al-Ghouti, D.A. Da'ana, Guidelines for the use and interpretation of adsorption
996 isotherm models: A review, J Hazard Mater, 393 (2020) 122383.
997 [88] C. Carucci, N. Scalas, A. Porcheddu, M. Piludu, M. Monduzzi, A. Salis, Adsorption and
998 Release of Sulfamethizole from Mesoporous Silica Nanoparticles Functionalised with
999 Triethylenetetramine, Int J Mol Sci, 22 (2021).
1000 [89] M. Ghanimati, M. Jabbari, A. Farajtabar, S.A. Nabavi-Amri, Adsorption kinetics and
1001 isotherms of bioactive antioxidant quercetin onto amino-functionalized silica nanoparticles
1002 in aqueous ethanol solutions, New J Chem, 41 (2017) 8451-8458.
1003 [90] J. Wang, X. Guo, Adsorption isotherm models: Classification, physical meaning,
1004 application and solving method, Chemosphere, 258 (2020) 127279.
1005 [91] V.-P. Dinh, N.-C. Le, L.A. Tuyen, N.Q. Hung, V.-D. Nguyen, N.-T. Nguyen, Insight
1006 into adsorption mechanism of lead(II) from aqueous solution by chitosan loaded MnO2
1007 nanoparticles, Mater Chem Phys, 207 (2018) 294-302.
1008 [92] W.A. Talavera-Pech, A. Ávila-Ortega, D. Pacheco-Catalán, P. Quintana-Owen, J.A.
1009 Barrón-Zambrano, Effect of functionalization synthesis type of amino-MCM-41 mesoporous

silica nanoparticles on Its RB5 adsorption capacity and kinetics, Silicon, 11 (2018) 1547-1555.
[93] A.H. Karim, A.A. Jalil, S. Triwahyono, S.M. Sidik, N.H. Kamarudin, R. Jusoh, N.W. Jusoh, B.H. Hameed, Amino modified mesostructured silica nanoparticles for efficient adsorption of methylene blue, J Colloid Interface Sci, 386 (2012) 307-314.
[94] M. Anbia, S.A. Hariri, Removal of methylene blue from aqueous solution using nanoporous SBA-3, Desalination, 261 (2010) 61-66.
[95] I. Gulcin, Antioxidant activity of food constituents: An overview, Arch Toxicol, 86 (2012) 345-391.
[96] I.G. Munteanu, C. Apetrei, Analytical methods used in determining antioxidant activity: A review, Int J Mol Sci, 22 (2021).
[97] F. Arriagada, G. Gunther, J. Morales, Nanoantioxidant-based silica particles as flavonoid carrier for drug delivery applications, Pharmaceutics, 12 (2020).
[98] Y. Deligiannakis, G.A. Sotiriou, S.E. Pratsinis, Antioxidant and antiradical SiO2 nanoparticles covalently functionalized with gallic acid, ACS Appl Mater Interfaces, 4 (2012) 6609-6617.
[99] G. Berlier, L. Gastaldi, E. Ugazio, I. Miletto, P. Iliade, S. Sapino, Stabilization of quercetin flavonoid in MCM-41 mesoporous silica: positive effect of surface functionalization, J Colloid Interface Sci, 393 (2013) 109-118.
[100] J. Xie, K.M. Schaich, Re-evaluation of the 2,2-diphenyl-1-picrylhydrazyl free radical (DPPH) assay for antioxidant activity, J Agric Food Chem, 62 (2014) 4251-4260.
[101] C. Cheignon, M. Tomas, D. Bonnefont-Rousselot, P. Faller, C. Hureau, F. Collin, Oxidative stress and the amyloid beta peptide in Alzheimer's disease, Redox Biol, 14 (2018) 450-464.
[102] D.A. Butterfield, A.M. Swomley, R. Sultana, Amyloid beta-peptide (1-42)-induced oxidative stress in Alzheimer disease: Importance in disease pathogenesis and progression, Antioxid Redox Signal, 19 (2013) 823-835.
[103] C. Hureau, P. Dorlet, Coordination of redox active metal ions to the amyloid precursor protein and to amyloid-β peptides involved in Alzheimer disease. Part 2: Dependence of Cu(II) binding sites with Aβ sequences, Coord Chem Rev, 256 (2012) 2175-2187.
[104] S. Khokhar, R.K. Owusu Apenten, Iron binding characteristics of phenolic compounds: Some tentative structure–activity relations, Food Chem, 81 (2003) 133-140.
[105] J. Liu, C. Detrembleur, M.C. De Pauw-Gillet, S. Mornet, C. Jerome, E. Duguet, Gold nanorods coated with mesoporous silica shell as drug delivery system for remote near infrared light-activated release and potential phototherapy, Small, 11 (2015) 2323-2332.
[106] G. Liu, H. Liang, Y. He, L. Lu, L. Wang, P. Liu, K. Cai, A nanoplatform based on mesoporous silica-coated gold nanorods for cancer triplex therapy, J Mater Chem B, 8 (2020) 9686-9696.
[107] V.A. Khanadeev, A.V. Simonenko, O.V. Grishin, N.G. Khlebtsov, One-shot laser-Pulse modification of bare and silica-coated gold nanoparticles of various morphologies, Nanomaterials (Basel), 13 (2023).
[108] J.G. Croissant, T.M. Guardado-Alvarez, Photocracking silica: Tuning the plasmonic photothermal degradation of mesoporous silica encapsulating gold nanoparticles for cargo release, Inorganics, 7 (2019).
[109] Y. Zhang, X. Zhan, J. Xiong, S. Peng, W. Huang, R. Joshi, Y. Cai, Y. Liu, R. Li, K. Yuan, N. Zhou, W. Min, Temperature-dependent cell death patterns induced by

functionalized gold nanoparticle photothermal therapy in melanoma cells, Sci Rep, 8 (2018) 8720.